Additive Manufacturing 99 (2025) 104659

Contents lists available at ScienceDirect

Additive Manufacturing

journal homepage: www.elsevier.com/locate/addma

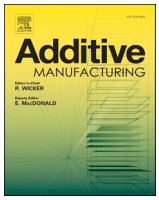

Modeling and spatio-temporal optimization of grayscale digital light processing 3D-printed structures with photobleaching resins

Xiru Fan [a,b,1], Mengjie Zhang [a,b,1], Liguo Hu [a,b], Le Dong [a,b], Qinghua Yu [a,b], Biao Zhang [c], Kun Zhou [d], Dong Wang [a,b,*]

[a] State Key Laboratory of Mechanical System and Vibration, School of Mechanical Engineering, Shanghai Jiao Tong University, Shanghai 200240, China
[b] Meta Robotics Institute, Shanghai Jiao Tong University, Shanghai 200240, China
[c] Frontiers Science Center for Flexible Electronics (FSCFE), Institute of Flexible Electronics (IFE), Northwestern Polytechnical University, 127 West Youyi Road, Xi'an 710072, China
[d] Singapore Centre for 3D Printing, School of Mechanical and Aerospace Engineering, Nanyang Technological University, Singapore 639798, Singapore

ARTICLE INFO

Keywords:
Grayscale DLP 3D printing
Spatio-temporal optimization
Microfluidic channel
Stair-stepping effect
Subpixel feature

ABSTRACT

Grayscale digital light processing (DLP) 3D printing modulates light intensity in each pixel through grayscale values, offering a promising approach for achieving high-resolution printed structures. However, existing theoretical models and optimization methods typically rely on the assumuption of a photo-invariant resin, for simplification. This study demonstrates that the curing depth varies even when the total accumulated dose remains constant, indicating a photo-variant effect. To address this, a spatio-temporal optimization method along with a model are developed, incorporating photobleaching effects, multilayer exposure, and Gaussian beam propagation. The model accurately predicts variations in curing depths at constant doses. Structures are optimized using this model, resulting in several significant improvements: channel heights are reduced to approximately one-fifth of the empirical minimum value with variations below 10 %; concave lenses are optimized with smooth surfaces; and the stair-stepping effect is notably reduced. Additionally, an asymmetric stair-stepping effect is identified between the left and right sides of objects printed at the corner, primarily caused by light divergence. The developed model and spatio-temporal optimization algorithm pave the way for high-fidelity grayscale DLP 3D printing.

1. Introduction

Digital light processing (DLP) 3D printing is a type of vat photopolymerization method that projects masked UV patterns to cure entire layers of resin [1–6]. Various strategies have been developed to enhance the precision of printed structures, including modifications to material compositions [7–10], advancements in printing equipments [11–15], and empirical optimization of printing parameters [16,17]. Despite these advancements, these methods alone are insufficient to address certain fundamental challenges because they do not involve adjusting the light field. These challenges include fabricating subpixel features, reducing stair-stepping effects, and overcoming empirical height limitations on channels.

One promising approach is grayscale DLP 3D printing, which modulates the intensity of light at each pixel to achieve high-resolution printed structures [18–21]. The design of the grayscale field in DLP 3D printing requires accurate theoretical models and inverse optimization algorithms due to the vast design space involved. Existing models range from reaction-diffusion models that consider detailed chemical processes to models based on the Beer-Lambert law and complex physical phenomena models implemented in finite element software [22–28]. To faciliate inverse optimization, a commonly adopted assumption is that the resin is photo-invariant, with its absorption properties remaining unchanged during photopolymerization. This assumption allows the printed depth to be analytically determined, facilitating inverse optimization and leading to the conclusion that curing depth remains consistent when the projection dose is the same. However, the photo-invariant assumption is not valid for many photopolymer resins,

* Corresponding author at: State Key Laboratory of Mechanical System and Vibration, School of Mechanical Engineering, Shanghai Jiao Tong University, Shanghai 200240, China.
E-mail address: wang_dong@sjtu.edu.cn (D. Wang).
[1] X.F. and M.Z. contributed equally to this work.

https://doi.org/10.1016/j.addma.2025.104659
Received 19 September 2024; Received in revised form 14 January 2025; Accepted 14 January 2025
Available online 15 January 2025
2214-8604/© 2025 Elsevier B.V. All rights are reserved, including those for text and data mining, AI training, and similar technologies.

as photoinitiators or photoabsorbers absorb photons and become inactive, a phenomenon known as photobleaching.

Incorporating the photobleaching effect into theoretical modeling is essential but challenging. This effect indicates that the attenuation coefficient of light intensity becomes a time-dependent function, that transforms the partial differential equations in the photodynamics model—one in the spatial domain and the other in the time domain—-from uncoupled to coupled equations, thereby complicating both the theoretical modeling and the inverse optimization processes. Previous studies have investigated the variation in cured depth under different manufacturing parameters, as well as their influence on minimum cure energy and penetration depth. For instance, an interlaboratory study identified significant variability in working curve data, critical cure energy, and penetration depth [29]. The cured depth of a polymerized gel network has been studied both experimentally and theoretically, with results showing that the photoinitiator concentration influences the curing depth and shrinkage under constant photonic energy [30]. Variations in light intensity and wavelength have also been shown to affect minimum cure energy, penetration depth, and printing accuracy by altering the photoinitiator decomposition rate [31,32].

Additionally, accurate modeling must account for multilayer exposure, Gaussian beam distribution, and light divergence. Multilayer exposure, often overlooked, causes penetrated light to cure not only the current layer but also previous layers. Experiments reveal that the light intensity within a single beam is non-uniform and follows a Gaussian distribution. Light divergence indicates that beams from the Digital Micromirror Device (DMD) do not travel in parallel but instead spread in convergent and divergent patterns. Incorporating these phenomena further complicates the theoretical models.

This work demonstrates that the curing depth varies with projection time and light intensity, even when the total accumulated dose remains constant. Fig. 1(a) plots the experimental curing depth (Z_f) against different accumulated light doses (D) with varying exposure times (t). The curing depth Z_f can vary even for the same accumulated dose. Additionally, the data points do not collapse into a single curve, indicating the influence of the photobleaching effect. To illustrate this phenomenon, a theoretical model is developed that incorporates photobleaching, multilayer exposure, Gaussian beam distribution, and light divergence. Given the vast design space of grayscale values, a spatio-temporal optimization algorithm is developed that operates on a grid finer than the pixel resolution in the x-y plane and within a time interval smaller than the exposure time. Using this method, the following results are achieved: (i) microfluidic channels, not constrained to integral multiples of the layer thickness, surpass the penetration depth limit, with variations remaining below 10 %; (ii) concave lenses are optimized with smooth surfaces; (iii) the stair-stepping effect is optimized, reducing the average roughness of the lateral profile to about one-third of its original value. The developed model and spatio-temporal optimization algorithm pave the way for high-fidelity DLP 3D printing using grayscale values.

2. Theoretical modeling

Fig. 1(b) shows the schematic of grayscale DLP 3D printing, where grayscale patterns are projected onto liquid resin, curing it layer by layer. The intensity of the projected UV light on each pixel is determined by grayscale values, denoted as g, that range from 0 to 1. Here, $g = 0$ represents an entirely black image with zero light intensity, and $g = 1$ corresponds to full light intensity. Polymerization is typically quantified by ϕ [19,23], a unitless quantity characterizing the percentage of reacted doubled bonds. When the gel point ϕ_c is reached, the liquid resin is considered to have transformed into a solid state. The theoretical model is developed below. The photopolymerization dynamics are described using the Beer-Lambert Law, incorporating the photobleaching effect, multilayer exposure, and Gaussian beam propagation.

2.1. Multilayer photoplymerization with photobeaching effect

The rate of change of ϕ is proportional to the light intensity $I$and the fraction of material available for conversion $[1 - \phi(x,y,z,t)]$ as [33]

$$\frac{\partial\phi(x,y,z,t)}{\partial t} = K\left[1-\phi\left(x,y,z,t\right)\right]I\left(x,y,z,t\right), \tag{1}$$

where K represents the overall reaction conversion rate. The light absorption within the resin follows the Beer-Lambert Law:

$$\frac{\partial I(x,y,z,t)}{\partial z} = -\overline{\mu}\left(x,y,z,t\right)I\left(x,y,z,t\right). \tag{2}$$

where$\overline{\mu}(x, y, z, t)$is the effective attenuation coefficient. The photoinitiators become inactive once they absorb photons, form radicals and get consumed in the reaction. In contrast, the photoabsorbers are not consumed in the reaction. Thus, $\overline{\mu}(x,y,z,t)$ is assumed as

$$\overline{\mu}(x,y,z,t) = \mu_0[1-\phi(x,y,z,t)] + \mu_\infty\phi(x,y,z,t) + \widehat{\beta}, \tag{3}$$

It is calculated as the weighted average between the attenuation coefficients of the uncured monomer (μ_0) and cured polymer material (μ_∞), weighted by their respective concentrations, and the absorption of the photoabsorber $\widehat{\beta}$.

For a photo-invariant resin, $\mu_0 = \mu_\infty = \overline{\mu}$, and Eqs. (1) and (2) are uncoupled. The analytical solution of curing depth Z_f can be obtained as $Z_f = \frac{1}{\mu}\ln\left(KI_0t/\ln\left(\frac{1}{1-\phi_c}\right)\right)$, where I_0 is the initial light intensity at $z = 0$. It indicates that the curing depth is influenced solely by the projection dose I_0t and not by the curing time. However, for photobleaching resin, the material becomes progressively transparent to UV radiation $\mu_0 > \mu_\infty$. Thus the two partial differential Eqs. (1) and (2) are coupled, and analytical solutions are difficult to obtain.

Through the integration of Eq. (1), $\phi(x,y,z,t)$ for a single exposure can be written in the following form:

$$\phi\left(x,y,z,t\right) = 1-\exp\left[-K\int_0^t I(x,y,z,t)\mathrm{d}t\right]. \tag{4}$$

For multi-exposure, $\phi(x,y,z,t)$ can be calculated by recursively adding $\phi(x,y,z,t)$ from each single exposure as [19,34] (Section S1 of the Supporting Information)

$$\phi\left(x,y,z,t_n\right) = 1-\exp\left[-\sum_{m=1}^{n}K\int_{t_{m-1}}^{t_m} I(x,y,z,t)\right]. \tag{5}$$

2.2. Gaussian beam propagation

Gaussian beam propagation is used to model the light distribution and its behavior during propagation, assuming that the intensity distribution of the beam from a single pixel follows a symmetric 2D Gaussian function [35]. At the focal plane ($z = 0$), the light intensity distribution is expressed as

$$I\left(x,y,z=0\right) = I_0\exp\left(-2\left[\frac{(x-x_0)^2+(y-y_0)^2}{\omega_0^2}\right]\right), \tag{6}$$

where I_0 is the peak amplitude of the Gaussian beam at the center (x_0, y_0), and ω_0 represents the beam's half-width at which the intensity drops to $1/e^2$ of I_0.

An ideal Gaussian beam maintains its Gaussian shape during propagation, with its waist changes with the distance from the focal plane. Fig. 1(c) shows the evolution of a Gaussian beam beyond $z = 0$. The waist $\omega(z)$ varies along the propagation direction, characterized by $\omega(z) = \omega_0\sqrt{1+(z/z_R)}$, where$z_R = \pi\omega_0^2/\lambda$ is the Rayleigh range, and λ representing the wavelength of the beam. The maximum intensity of the light decreases with increasing propagation distance, resulting from the spreading of the light beam. As the beam propagates, the Gaussian

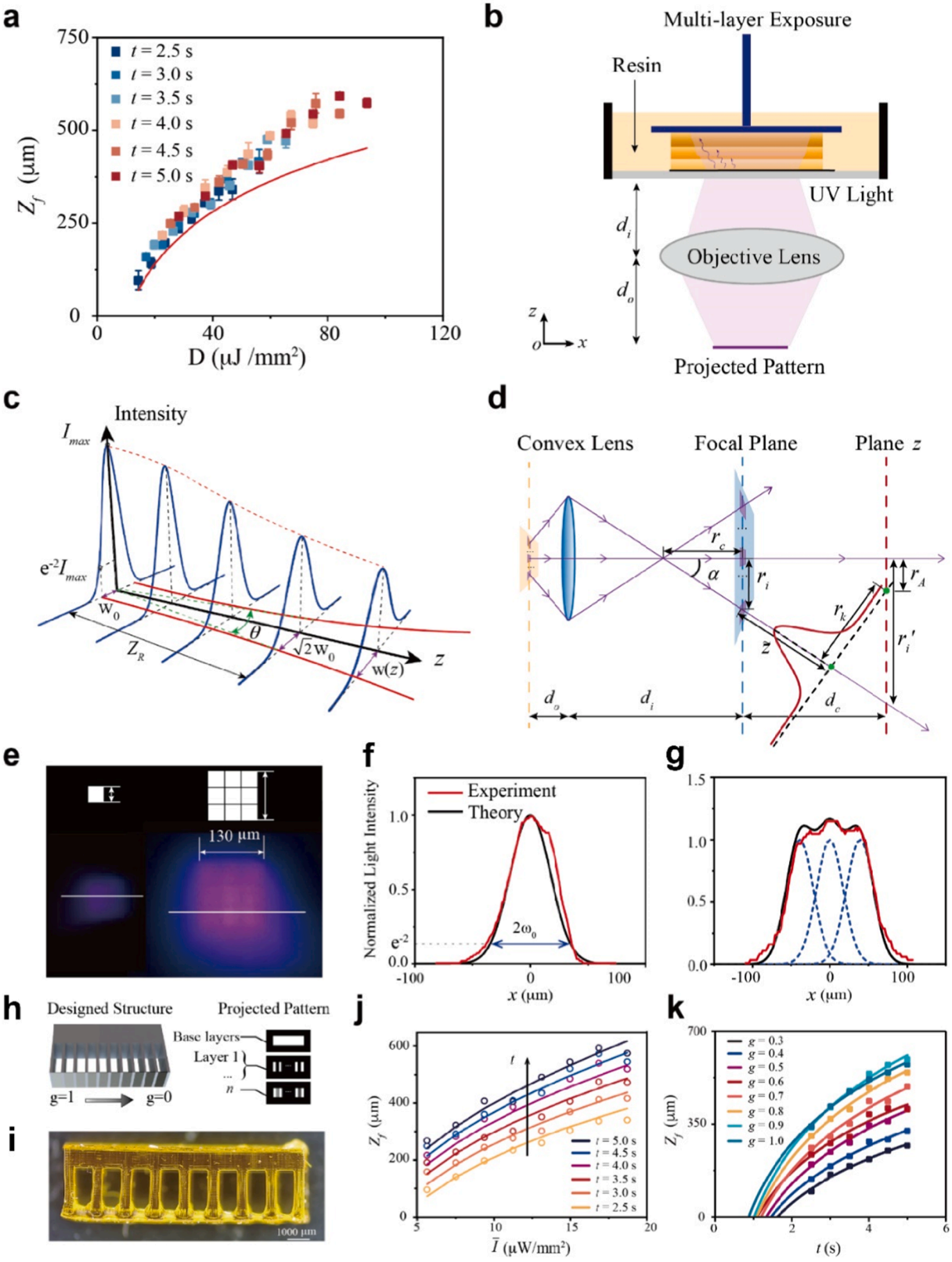

Fig. 1. Grayscale DLP 3D printing with photobleaching effect. (a) The dependence of the experimental curing depth Z_f on the accumulated dose D. The red curve represents the model prediction with photo-invariant assumption. (b) Multilayer photopolymerization: UV light penetrates the front layer, resulting in over-curing of subsequent layers. (c) Gaussian beam propagation: the beam width increases and intensity decreases along the z-axis. (d) Gaussian beam convergence and divergence. (e) Light intensity captured by a single pixel versus a 3 × 3 pixel array. (f) Experimental and theoretical normalized light intensity distribution of a single pixel. (g) Experimental and theoretical normalized light intensity distribution of a 3 × 3 pixel array. (h) The designed U-shaped structure, its sliced image, and (i) the printed structure cured with different grayscale values g. (j) Comparison of the experimental (markers) and theoretical (solid curves) Z_f. (k) Experimental and fitted cure depth Z_f against exposure time t for g ranging from 0.3 to 1. Intercepts indicates the critical exposure times.

intensity profile also becomes wider, but the total energy (the area under the curve) remains constant.

During propagation, the energy loss primarily occurs due to reflection at membrane interface. Thus, the intensity distribution of the i-th pixel at a distance z from the focal plane is expressed as

$$I_i(x,y,z) = (1-\widehat{\alpha})p(x,y,z)I_i(x,y,z=0), \tag{7}$$

where $\widehat{\alpha}$ is the reflection coefficient, denoting the ratio of light reflected by the interfaces. The amplitude factor $p(x, y, z)$ is defined as

$$p\left(x,y,z\right) = \left(\frac{\omega_0}{\omega(z)}\right)^2 \exp\left[-2\left((x-x_0)^2+(y-y_0)^2\right)\left(\frac{1}{\omega(z)^2}-\frac{1}{\omega_0^2}\right)\right]. \tag{8}$$

Additionally, Gaussian beams reflected from a DMD are not parallel. They initially diverge, converge through a lens, and subsequently diverge again past the focal plane [23]. Fig. 1(d) illustrates the light propagation through the objective lens and across the focal plane. The light intensity $I(x, y, z)$ at any point (x, y) on the z plane is the superposition of the effects of all the light beams: $I(x,y,z) = \sum I_i(x,y,\widetilde{z})$, where $\widetilde{z}$is the actual propagation distance given by $\widetilde{z} = z/\cos\alpha_i - r_k \tan\alpha_i$. Here, $r_k = (r_i' - r_A)\cos\alpha_i$ and it is the projection distance from the center of a Gaussian beam to a particular point on the focal plane. r_A is the distance from $A(x, y, z)$ to the central axis. The geometric relationship requires $r_c = d_c r_i/(r_i' - r_i)$, where r_i and r_i' represent the distance of the light beam i to the central axis on the focal plane and plane z, respectively. Furthermore, d_c denotes the distance between the plane z and the focal plane, and r_c is the distance from the convergent point to the focal plane. The divergent angle for this Gaussian beam can be calculated using $\tan\alpha_i = r_i/r_c$.

3. Experiments

3.1. Grayscale 3D printing

A grayscale DLP printing system has been developed that composed of a UV-projector (DLi 3DLP9000, with a 405 nm UV-light source and a DMD module), a beam splitter, a resin tank with a transparent glass window coated with PDMS membrane, and a linear translation stage. The resolution of the projector is 2560 pixels × 1600 pixels. Before printing, the CAD model is sliced into images with the desired layer thickness. The grayscale value for each pixel is assigned based on the desired material distribution using MATLAB code.

3.2. Materials

The photocurable elastomer TangoPlus, purchased from Stratasys (MN, USA), is selected as the base material. Ebecryl 113 was purchased from Allnex (Germany). Ebecryl 113 is an aliphatic monofunctional acrylate. The photoabsorber Sudan I was purchased from Sigma-Aldrich (MO, USA). All the materials are used without any further modification. The hybrid resin (TEAA) is prepared by adding Ebecryl 113 to the commercial UV-curable resin TangoPlus in a weight ratio of 4:6. The hybrid resin is thoroughly blended for 1 min at 2000 rpm, followed by centrifugation at 2200 rpm for 1 min using a planetary centrifugal mixer (ARE-310, Thinky, USA). 0.02 wt% Sudan I was added to this mixture at room temperature. After adding Ebecryl 113, the fracture strain increses from approximately 120–200 % [36]. Although TangoPlus contain absorbers, Sudan I is added to enhance the printing resolution. The viscosities of TangoPlus and TEAA are measured as 109 mPa•s and 115 mPa•s, respectively.

To characterize the material's glass transition, DMA tests (TA Instruments, Model Q850) are conducted on rectangular samples (Fig S19 of the SI) with dimensions of 12.3 mm× 6.2 mm × 1.3 mm. During the experiment, the temperature was increased from −75 °C to 75 °C at a rate of 3 °C/min. The Tg of the material is around 10 °C. When the temperature changes from −75 °C to 75 °C, the storage modulus changes from approximately 2 GPa to 0.5 MPa.

3.3. Light field measurement

The light intensities were measured for a single pixel and a 3 × 3 array (Fig. 1(e)). The projected image is captured using Sony-ILCE-7M3 with a Laowa 25 mm f/2.8 2.5–5X Ultra Macro lens. The length of a single camera pixel has been calibrated as 1.06 μm. The length of a single pixel of the light engine on the focal plane is calculated as 43 μm. The light intensity follows Gaussian distribution (Fig. 1(f) and (g)) and the half-width of Gaussian beam$\omega_0 = 30$μm.

3.4. Theoretical model validation

Experiments were conducted to validate the theoretical model. The dependence of light intensity on g was also measured (Section S3 of the Supporting Information). The parameters $\widehat{\alpha}$ and $\widehat{\beta}$ were experimentally determined as 0.316 and 0.228 mm^{-1}, respectively (Section S13 of the Supporting Information). A U-shaped structure was fabricated, with the design and sliced images shown in Fig. 1(h) and (i). The experimental procedure involved curing ten base layers for 3.5 seconds at full light intensity, followed by printing nine pillars with 20 layers each. A single layer was cured with g varying from 0.3 to 1 between the pillars. The thickness Z_f of this layer was measured. Samples were fabricated with different exposure times (t = 2.5–5 s), and two samples were printed for each exposure time to ensure repeatability.

The theoretical model was used to fit the experimental data. The fitted parameters are $K = 0.021\ mm^2\mu W^{-1}$ and $\mu_0 = 5.44\ mm^{-1}$. The solid/liquid interface is determined as the position where ϕ reaches ϕ_c [33]. The parameter μ_∞ is set to 0 as the photoinitiators are consumed during the reaction, while $\widehat{\beta} = 0.228\ mm^{-1}$ represents the unconsumed photoabsorbers, which is in an order of magnitude smaller than μ_0. The experimental depths are also fitted with the theoretical model assuming $\widehat{\beta} = 0$. A comparison of the experimental and theoretical Z_f values as a function of light intensities is shown in Figure S16. Both models accurately estimate Z_f, but to simplify calculations, the theoretical model with $\widehat{\beta} = 0$ is adopted for subsequent optimizations.

Fig. 1(j) compares the theoretical and experimental heights of Z_f versus light intensities under different curing times. The theoretical model agrees well with the experimental data. The experimental data can also be used to determine ϕ_c. Fig. 1(k) plots Z_f against exposure time t for g ranging from 0.3 to 1. Curve fitting was performed using a logarithmic function, and the curve was extrapolated to the x-axis to determine the intercepts, which represent the critical exposure times. These critical exposure times are shown in Table S4. Subsequently, the developed theoretical model was utilized to calculate ϕ at varying depths within the resin. The maximum and mean ϕ values at the bottom plane are also tabulated in Table S4. The mean ϕ serves as a valuable indicator for estimating ϕ_c. Based on these results, ϕ_c can be set at 0.15. Notably, the mean ϕ_c consistently remains around 0.15 for g ranging from 0.7 to 1.

4. Optimization

The validated theoretical model is used to optimize the printed structures. Due to the variation of $\overline{\mu}$ throughout the DLP printing process, the optimization method necessitates discretization not only in the spatial domain but also in the time domain.

4.1. Spatio and temporal discretization

Discretization is performed in both the spatial and temporal domains. Spatially, two resolution scales are utilized. The first, referred to as the normal space, is depicted in Fig. 2(a) and comprises dimensions of

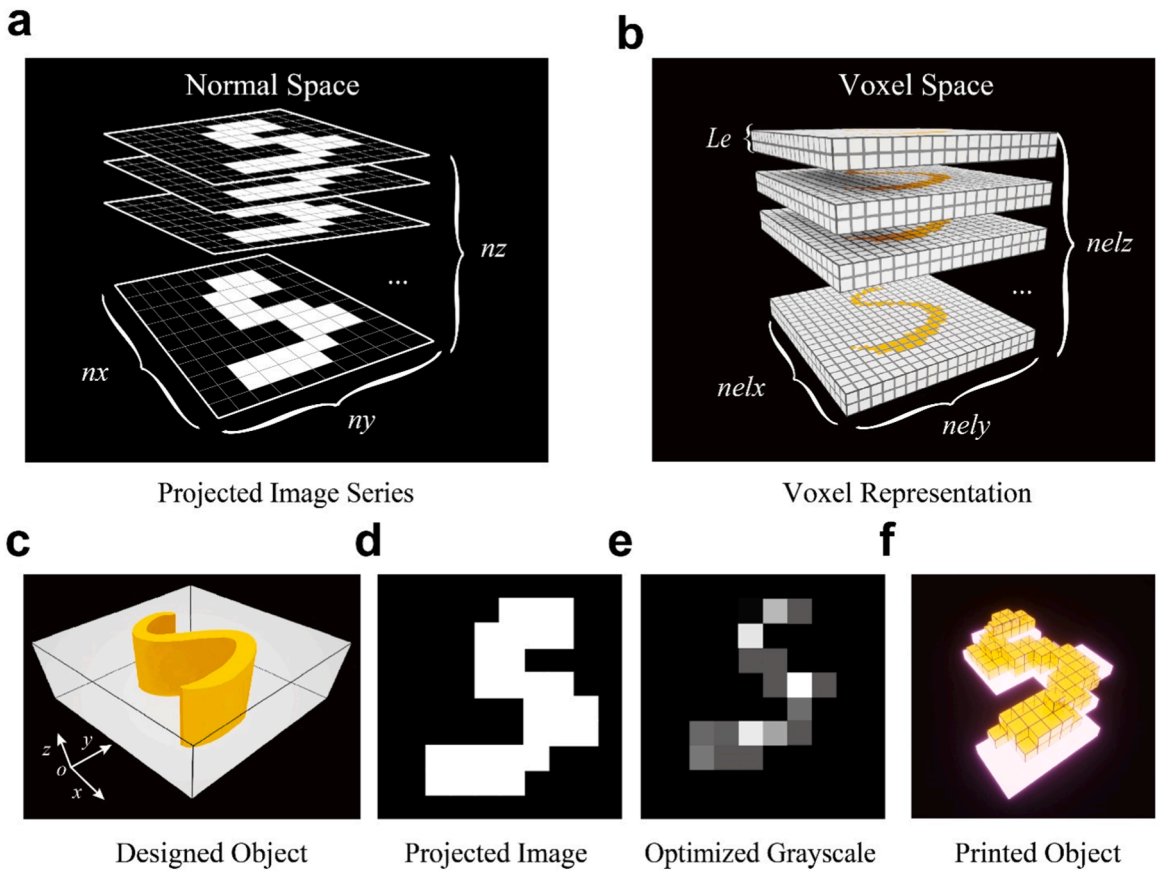

Fig. 2. Optimization procedures. (a) Sliced images of a objective model (normal space) and the representation of g_s. (b) Voxel representation of the objective model (voxel space) and the representation of P_r. (c) Objective model of a handwritten letter "S". (d) Sliced images of the objective model. (e) Optimized grayscale image. (f) Schematic of the cured layer.

$nx \times ny \times nz$. Here, nx and ny represent the number of pixels along the x and y axes of the projected image, respectively, and nz is the number of sliced layers. Each element in the normal space is further discretized into $Nx \times Ny \times Nz$ voxels within a finer resolution space. Thus, the dimensions of this finer voxel space are defined as $nelx \times nely \times nelz$, where $nelx = nx \times Nx$, $nely = ny \times Ny$, and $nelz = nz \times Nz$ (Fig. 2(b)). A column of pixels from a series of projected images is denoted as g_s, as shown in Fig. 2(b).

Eq. 5 establishes the dependency of $\phi(x, y, z, t)$ on light intensity I (x, y, z, t) and material parameter K. Light intensity, I (x, y, z, t) undergoes attenuation along the z-axis, as dictated by Eqs. 2 and 3, and is nonlinearly related to the projected light dose. This relationship necessitates a spatial and temporal discretization of Eq. 5 to correlate $\phi(x, y, z, t)$ with the light dose at each exposure, that can be represented in the matrix form

$$[\varphi] = [T] \cdot [d], \tag{9}$$

where φ is a photopolymerization process variable defined as $\varphi = \ln(1-\phi)$ to linearize the multi-exposure model, d represents the exposure dose, T is the transmission matrix, and $[\bullet]$ represents the corresponding matrix form. As light penetrates along the vertical direction, the matrix equation is solved sequentially for each column of voxels. Consequently, Eq. 9 for a specific voxel column P_r becomes

$$[\varphi]^{P_r} = [T]^{P_r} \cdot [d]^{P_r}. \tag{10}$$

In the voxel space, there are $nelx \times nely$ columns of voxels, where P_r represents the r^{th} column ($r = 1, 2, \ldots, nelx \times nely$). The terms $[\varphi]^{P_r}$, $[T]^{P_r}$, $[d]^{P_r}$ represent the photopolymerization variable, transmission matrix, and nodal exposure dose for a column of voxels P_r, respectively. Furthermore, $[\varphi]^{P_r}$ is a $nelz \times 1$ vector, $[T]^{P_r}$ is a $nelz \times nelz$ matrix, and $[d]^{P_r}$ is a $nelz \times 1$ vector.

Eq. 10 is further discretized in the time domain. In the numerical implementation, ϕ from the previous step is used to calculate $\bar{\mu}$ at the current step for each voxel using Eq. 3. Detailed calculations are provided in Section S2 of the Supporting Information.

4.2. Optimization procedures

The optimization process is framed as an inverse problem aimed at minimizing the maximum discrepancy between the desired and the numerically calculated φ by adjusting g. Mathematically, the formulation is

$$\begin{aligned} &Obj. \min_{g} \left\{ \max [F] \right\}, F^{P_r} = \left\| [\varphi]^{P_r} - [\varphi_{obj}]^{P_r} \right\|^2 \\ &s.t. \quad 0 \le g_{\min} \le g \le 1, \end{aligned} \tag{11}$$

where $[\varphi_{obj}]^{P_r}$ represents the target φ for a column of voxels P_r, and $[F]$ is a $nelx \times nely$ matrix quantifying the error for every column of voxels. Each element F^{P_r} in $[F]$ is the sum of the squared errors between the φ_{obj} and φ for each voxel column P_r. The optimization seeks to adjust g to minimize the maximum error value within $[F]$.

To ensure manufacturability, each layer must reliably bond with the previous layers. To mitigate potential adhesion issues, a minimum grayscale value, $g_{\min}$, is imposed as a constraint in Eq. 11 and it is determined based on the minimum grayscale value necessary for a layer to adequately cure and adhere to the preceding layer. It is calculated based on specific exposure time and layer height. However, due to photobleaching effect, $g_{\min}$ cannot be explicitly expressed. Instead, it is

determined through an optimization process using $\varphi_{obj} = \varphi_c$. The resultant g from this optimization defines $g_{\min}$. Detailed procedures of calculating $g_{\min}$ are outlined in Section S8 of the Supporting Information. It is important to note that the constraints for $g_{\min}$ may vary for different cases.

The flowchart of the optimization procedure is illustrated in Figure S3. The grayscale matrix is updated at each iteration. Fig. 2(c) shows an objective model of a handwritten letter "S". The initial projected image of the n^{th} layer is shown in Fig. 2(d), and the optimized grayscale image of the n^{th} layer is depicted in Fig. 2(e). The schematic of the cured layer is shown in Fig. 2(f). The term, φ_{obj}, is in the range of $(-\infty, 0]$, wherein 0 is set for uncured voxels.

5. Applications

The theoretical model and optimization algorithm are used to design the ϕ distribution. Microfluidic channels, concave lenses, and reduced stair-stepping effects are demonstrated.

5.1. Microfluidic channel optimization

Micrometer-sized channels are challenging to print because the light

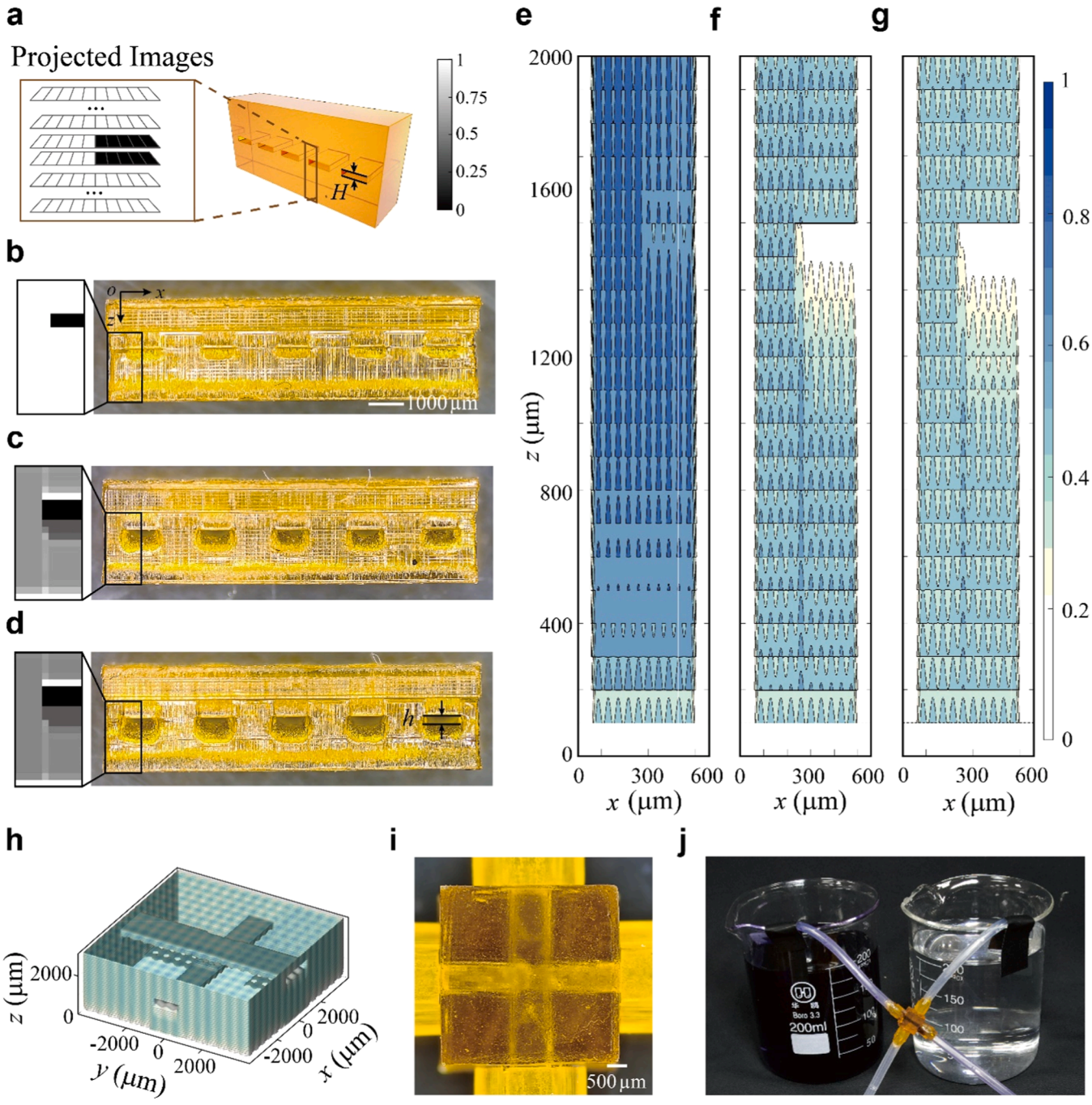

Fig. 3. Optimization of microfluidic devices. (a) Schematics of a structure with microfluidic channels. (b) Over-cured channels using unoptimized images. (c) Optimized grayscale images and printed structures with a height of $H = 100$ μm. (d) Optimized grayscale images and printed structures with a height of $H = 150$ μm. (e)-(g) Calculated ϕ distribution for (b)-(d). (h) Optimized ϕ distribution and (i) optical image of a microfluidic device with two independent channels. (j) Two liquids with different colors crossing the channels continuously without mixing.

penetrates the resin and cures the residual resin inside the flow channels, causing clogs [15,37]. The penetration depth of the current device and photopolymer resin is calculated to be approximately 212 μm (Section S6 of the Supporting Information). Previous studies indicate that the empirical minimum channel height for photocurable resins should be more than 2.3 times the light penetration depth [37], corresponding to 488 μm approximately. Using the developed model and optimization method, it has been demonstrated that microfluidic channels with a height of around one-fifth of this minimum can be successfully fabricated.

Fig. 3(a) shows a structure with five microfluidic channels. Fig. 3(b) displays the 3D printed structure, where $g = 0$ for the channel and 1 for other positions, with an exposure time of $t = 2$ s. Fig. 3(e) represents the predicted ϕ distribution. Both experimental results and theoretical predictions demonstrate that the channels are over-cured and blocked.

The optimized method was applied to print channels with heights $H = 100$ μm and 150 μm. The objective was set to achieve a uniform $\phi = 0.4$ across the structure, equivalent to $\varphi_{obj} = -0.51$. A positive φ_{obj} was set for the channels to achieve better-optimized results, as a positive φ_{obj} could never be reached. Fig. 3(f) and (g) show the theoretically optimized ϕ distributions, with the corresponding optimized grayscale images displayed beside them (SI Movie 1). The grayscale values remain consistent across most areas except in regions surrounding the channel. A distinct white layer appears above the channel, as no extra light penetrates from the sequential layers. Beneath the white layer are three black layers, attributed to the penetration depth of 212 μm and a layer height of 100 μm. Following these black layers is a dark gray region, which allows light to penetrate the current layer and cure the area directly beneath the channel. The size of this dark gray region depends on the channel height. A brighter vertical line near the channel

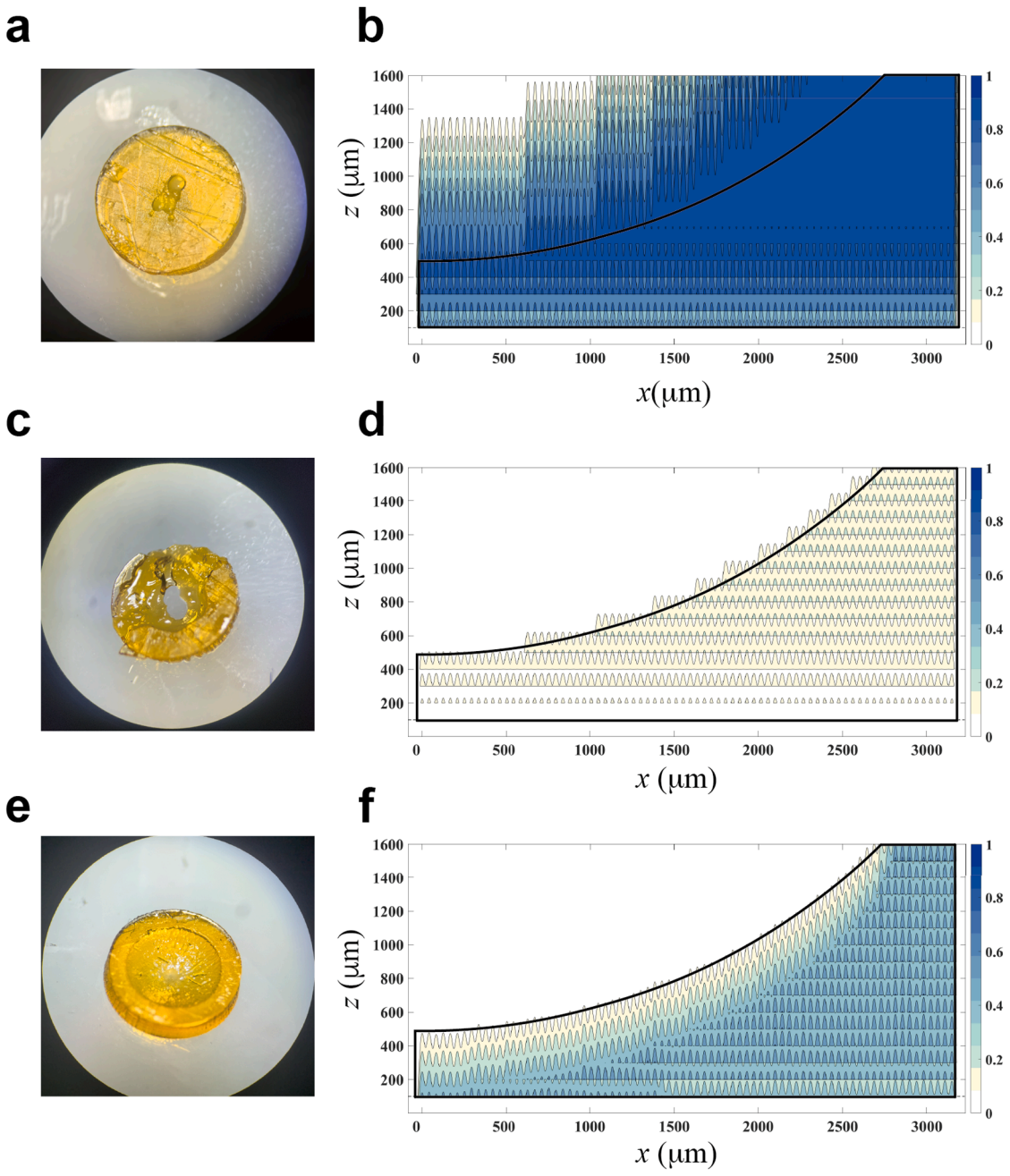

Fig. 4. Microscopic images and simulation results of concave lenses fabricated using different projected images: (a, b) binary images, (c, d) unoptimized grayscale images ($g = 0.5$), and (e, f) optimized grayscale images. Units: μm.

compensates for the black and dark gray regions.

Supplementary material related to this article can be found online at doi:10.1016/j.addma.2025.104659.

Microfluidic channels were printed using the optimized grayscale images (Fig. 3(c) and (d)), with two samples printed for each height. The height of the printed microfluidic channels was measured using a ZWSP-4KCH CCD camera. The average printed heights were 115 μm and 160 μm for designed heights of 100 μm and 150 μm, respectively. Additionally, microfluidic channels with heights of 250 μm and 300 μm were also printed, resulting in average printed heights of 264 μm and 312 μm, respectively (Figure S9). The variations in height were lower than 10 %. After fabrication, the printed structures were washed in ethanol for a few seconds to remove any uncured resin. They were not subjected to post-curing. The post-fabrication handling, including washing and curing, can influence the final dimensions of the printed structures. To minimize these potential effects, the processing

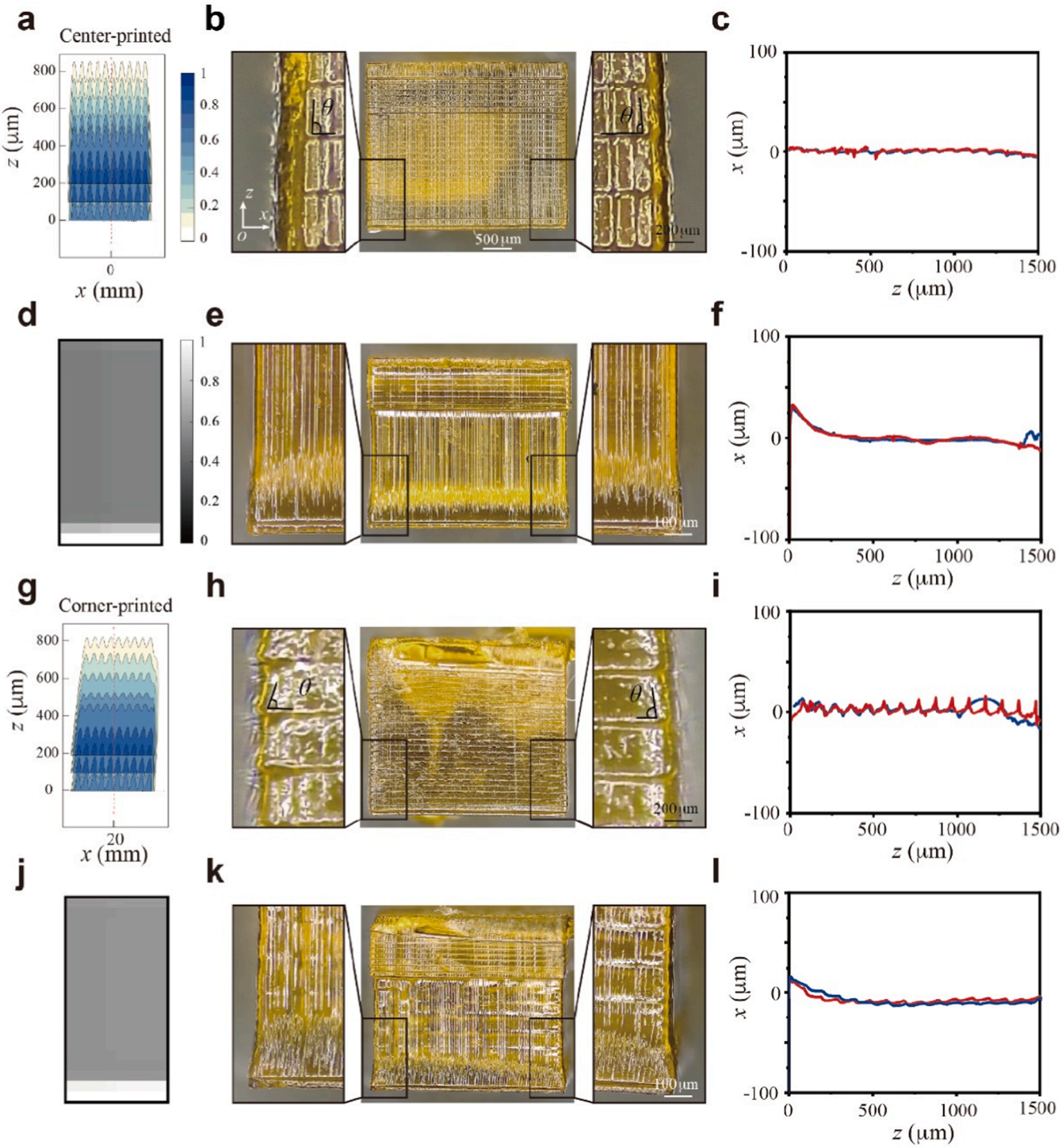

Fig. 5. Optimizing stair-stepping effect. (a)-(c) The theoretical ϕ distribution, optical image, and the lateral profile of unoptimized center-printed structures respectively. (d)-(f) The optimized grayscale image, optical image, and the lateral profile of optimized center-printed structures respectively. (g)-(i) The theoretical ϕ distribution, optical image, and the lateral profile of unoptimized corner-printed structures respectively. (j)-(l) The optimized grayscale image, optical image, and lateral profile of optimized corner-printed structures respectively. The red and blue curves denote the left and right edges of the experimental rectangles, respectively.

conditions are carefully controlled to ensure consistency.

A microfluidic device with two crossed channels, each with a height of 200 μm, was printed (Fig. 3(i)). The predicted contours with $\phi = \phi_c$ are shown in Fig. 3(h), clearly indicating the two channels. The optimized parameters are shown in Figure S8. The microfluidic device was tested by injecting two liquids with different colors into the inlets. The liquids continuously crossed the channels without mixing (Fig. 3(j) and SI Movie 2). While microfluidic channels of this scale can be fabricated using various existing techniques, this study uses a theoretical model and inverse optimization to enable the precise printing of channels that surpass the traditional penetration depth limit, demonstrating an advancement in DLP 3D-printed microfluidic devices.

Supplementary material related to this article can be found online at doi:10.1016/j.addma.2025.104659.

5.2. Optimization of concave lenses

Fig. 4 shows the optimization of concave lenses. Fig. 4(a), (c), and (e) depict the microscopic images of the printed concave lenses, while Fig. 4 (b), (d), and (f) show the simulated degree of conversion distribution for half of the cross-section. The black curve outlines the designed profile. In Fig. 4(a), the lens printed using binary patterns is overcured, which aligns well with the simulation result shown in Fig. 4(b). The lens printed with unoptimized grayscale patterns is undercured, leading to a hole at the center (Fig. 4(c)). The simulation in Fig. 4(d) shows a low degree of conversion in the structure, with some regions falling below the gel point. In contrast, the lens printed using optimized grayscale patterns accurately preserves the designed curvature (Fig. 4(e)). The corresponding simulation in Fig. 4(f) demonstrates high fidelity, confirming the effectiveness of the optimization.

5.3. Reducing the stair-stepping effect

The stair-stepping effect is a prevalent issue that results in step-like ridges on the lateral profiles of printed structures [38]. This effect is particularly pronounced in bottom-up DLP 3D printing, where the polymerization degree ϕ at the lower part of each layer is typically much higher than at the upper part. Consequently, the bottom edge becomes wider than the top edge, leading to visible ridges. Achieving a uniform ϕ distribution is essential to mitigate this issue.

To investigate the stair-stepping effect, a theoretical model is employed to predict the ϕ distributions of a three-layer U-shaped structure printed with light beams from the center of the projector using binary images. Fig. 5(a) shows these predicted distributions, clearly revealing a symmetric stair-stepping effect. The $z = 0$ position corresponds to the last printed layer, where conversion is lower due to the absence of multilayer exposure. The layer above 300 μm is formed by light penetration. Thus, the conversion is highest between 200 and 300 μm.

Subsequently, a multilayer rectangular structure with dimensions of 80 pixels × 40 pixels was printed (Fig. 5(b)). The printed structure exhibited a symmetric stair-stepping effect with measured inclined angles of approximately $\theta = 85°$ on both sides. Fig. 5(c) plots the experimental lateral profile of both the left (red) and right (blue) edges of the rectangles. The surface roughness values R_a and R_z are calculated and presented in Table S1 to quantitatively assess the stair-stepping effect. Here, R_z represents the maximum height difference within a typical layer, while R_a is the corresponding standard deviation.

To mitigate the stair-stepping effect, the developed optimization method was employed with the objective of achieving a uniform $\phi = 0.5$. The optimization method effectively reduced the stair-stepping effect, as demonstrated in Fig. 5(d) and (e). The optimized structures have an average inclined angle of $\theta = 88°$, which is nearly vertical. The lateral profile of the optimization rectangles (Fig. 5(f)) exhibit a significant reduction in roughness compared to those printed normally. For example, R_z was reduced from 5.7 μm to 1.3 μm on the left side and from 4.3 μm to 1.1 μm on the right side. Similarly, R_a was reduced from 1.1 μm to 0.34 μm on the left side and from 1.0 μm to 0.61 μm on the right side.

Additionally, an asymmetric stair-stepping effect was observed in rectangles printed at the corner of the build platform. Fig. 5(g) shows the predicted ϕ distributions of a three-layer rectangle printed using binary images at the top-right corner, positioned 320 pixels by 200 pixels away from the projector's center. Unlike the symmetric effect seen in centrally printed rectangles, the corner-printed rectangle shows asymmetry due to light divergence. The light beam diverges towards the right, reducing the stair-stepping effect on the right edge while intensifying it on the left. Figure S12 plots the theoretical light intensity for different planes ($z = 0$, 500 μm, and 1000 μm). Beyond the focal plane, the light intensity becomes asymmetric at the corner, with the intensity profile on the right side being steeper than that on the left (Fig. S12(b)). This asymmetry in the light intensity distribution results in asymmetric lateral profiles for the left and right edges of the rectangles printed at the corner of the projection area.

This is confirmed by experimental validations, with $\theta = 87°$ and 75° measured for the right and left sides, respectively (Fig. 5(h) and (i)). Quantitative roughness measurements show that R_a and R_z values for the right edge are typically an order of magnitude lower than those for the left edge (Table S2). This highlights the importance of considering light divergence in the printing process.

The developed modeling and optimization method can also optimize structures printed at the corners, as light divergence is incorporated into the theoretical model. Fig. 5(j)-(l) show the optimized g distribution, the structure printed using the optimized image pattern, and the corresponding lateral profiles respectively. The results demonstrate a significant reduction in the stair-stepping effect. For example, on the left side, R_z was reduced from 28.6 μm to 6.6 μm, and R_a is redcued from 4.4 μm to 1.6 μm.

6. Discussions and conclusions

Recently, significant effort has been devoted to advance the modeling of the grayscale DLP 3D printing process. One of the pioneering approaches is the reaction-diffusion model, that considers detailed chemical processes, including the initiation of free radicals, chain growth, and chain termination [25,26,39]. Another notable model is the multiphysics model, that incorporates a super-Gaussian description of the light field, photobleaching effects, heat generation, thermal strains, and chemical shrinkage [22,23]. While these models are highly accurate, inverse optimization is relatively challenging. To simplify the optimization process, the photo-invariant assumption is often used. For example, Guven *et al.* developed a voxel-based optimization method based on the photo-invariant assumption, considering the Gaussian light distribution and photodynamics [24]. Similarly, Bonada *et al.* developed an optimization procedure to increase vertical accuracy [40]. In contrast, this work does not delve into the detailed chemical processes. Instead, two partial differential equations are utilized to describe photodynamics while incorporating key factors including photobleaching effects, light divergence, and Gaussian beam propagation. This approach simplifies the inverse optimization process and facilitates the creation of high-fidelity structures. The theoretical model and optimization method can also be expanded to photoresins with different polymerization mechanisms. Specifically, the detailed photopolymerization kinetics can be incorporated into the Beer-Lambert law to account for different polymerization behaviors. The model should also be validated across multiple material systems, and 3D printed multi-material structures.

Utilizing the molar extinction coefficient could render the model more versatile and applicable to a broader range of photopolymer systems. However, TangoPlus is a mixed resin, and its detailed composition is not publicly available. Thus, the attenuation coefficient μ is used, which is easier to determine experimentally for this specific resin. In systems where the resin composition is well-defined, the molar

extinction coefficient would indeed be a more appropriate choice.

This work reveals that the curing depth for a single exposure varies with changes in projection time and light intensity, even though their product (the total accumulated dose) remains constant. This finding challenges the widely adopted photo-invariant assumption. To explain this phenomenon, a model for the grayscale DLP 3D printing process is developed, incorporating the photobleaching effect, Gaussian beam distribution, and light divergence. The inclusion of photobleaching results in coupled partial differential equations within the model, thereby rendering analytical solutions infeasible. Consequently, a spatio-temporal optimization algorithm has been designed that operates on a spatial grid finer than the optical resolution and temporal interval shorter than the exposure time for each layer, enabling the calculation of optimal grayscale values for high-fidelity printing.

The optimization method transcends traditional limitations on channel height. It successfully achieves channel heights approximately one-fifth of the empirical minimum height, with variations remaining below 10 %. Furthermore, this approach enables the fabrication of concave lenses and the reduction of stair-stepping effect. Additionally, an asymmetric stair-stepping effect has been observed, where the stair-stepping behavior differs between the left and right sides of the printed object. This asymmetry occurs when the object is printed at the corner rather than at the center of the projection area. This variation is primarily caused by light divergence, that affects the uniformity of light intensity. The developed model and spatio-temporal optimization algorithm pave the way for high-fidelity grayscale DLP 3D printing.

Code availability

The code used in this paper is available upon any reasonable request.

Author Statement

Xiru Fan: Methodology, Investigation, Data curation, Visualization, Formal analysis, Writing original draft **Mengjie Zhang**: Methodology, Investigation, Data curation, Visualization, Validation, Formal analysis; **Liguo Hu**: Methodology, Data curation, Validation, Visualization; **Le Dong:** Methodology; **Qinghua Yu:** Methodology, Data curation; **Biao Zhang:** Methodology, Writing - review &editing; **Kun Zhou**: Methodology, Writing - review &editing; **Dong Wang**: Conceptualization, Methodology, Formal analysis, Validation, Writing-original draft, Writing - review &editing, Resources, Project administration, Funding acquisition.

CRediT authorship contribution statement

Dong Wang: Writing – review & editing, Writing – original draft, Supervision, Conceptualization. **Kun Zhou:** Writing – review & editing, Supervision. **Mengjie Zhang:** Project administration, Methodology, Conceptualization. **Xiru Fan:** Writing – review & editing, Writing – original draft, Visualization, Validation, Software, Project administration, Methodology, Formal analysis, Conceptualization. **Biao Zhang:** Supervision, Conceptualization. **Qinghua Yu:** Methodology. **Le Dong:** Writing – review & editing, Visualization, Supervision, Conceptualization. **Liguo Hu:** Visualization, Validation, Methodology.

Declaration of Competing Interest

The authors declare that they have no known competing financial interests or personal relationships that could have appeared to influence the work reported in this paper.

Acknowledgements

D.W. acknowledges support from the National Natural Science Foundation of China (Grant No. 52275025), the National Key Research and Development Program of China (No. 2022YFB4700900), and the State Key Laboratory of Mechanical System and Vibration (Grant No. MSVZD202401).

Appendix A. Supporting information

Supplementary data associated with this article can be found in the online version at doi:10.1016/j.addma.2025.104659.

Data availability

No data was used for the research described in the article.

References

[1] J. Wu, et al., Rapid digital light 3D printing enabled by a soft and deformable hydrogel separation interface, Nat. Commun. 12 (2021) 6070.
[2] D. Wang, et al., Soft actuators and robots enabled by additive manufacturing, Annu. Rev. Control, Robot., Auton. Syst. 6 (2023) 31–63.
[3] X. Wan, et al., Recent Advances in 4D Printing of Advanced Materials and Structures for Functional Applications, Adv. Mater. (2024) 2312263.
[4] X. Zheng, et al., Ultralight, ultrastiff mechanical metamaterials, Science 344 (2014) 1373–1377.
[5] S. You, et al., High cell density and high-resolution 3D bioprinting for fabricating vascularized tissues, Sci. Adv. 9 (2023) eade7923.
[6] S. Li, et al., Digital light processing of liquid crystal elastomers for self-sensing artificial muscles, Sci. Adv. 7 (2021) eabg3677.
[7] Q. Ge, et al., 3D printing of highly stretchable hydrogel with diverse UV curable polymers, Sci. Adv. 7 (2021) eaba4261.
[8] M. Caprioli, et al., 3D-printed self-healing hydrogels via Digital Light Processing, Nat. Commun. 12 (2021) 1–9.
[9] S.H. Kim, et al., Precisely printable and biocompatible silk fibroin bioink for digital light processing 3D printing, Nat. Commun. 9 (2018) 1620.
[10] K. Kowsari, et al., Photopolymer formulation to minimize feature size, surface roughness, and stair-stepping in digital light processing-based three-dimensional printing, Addit. Manuf. 24 (2018) 627–638.
[11] C. Zhou, Additive manufacturing based on optimized mask video projection for improved accuracy and resolution, J. Manuf. Process. 12 (2012).
[12] J. Cheng, et al., Centrifugal multimaterial 3D printing of multifunctional heterogeneous objects, Nat. Commun. 13 (2022) 7931.
[13] H. Cui, et al., Design and printing of proprioceptive three-dimensional architected robotic metamaterials, Science 376 (2022) 1287–1293.
[14] Y. Xu, et al., Hopping light vat photopolymerization for multiscale fabrication, Small 19 (2023) 2205784.
[15] Y. Xu, et al., In-situ transfer vat photopolymerization for transparent microfluidic device fabrication, Nat. Commun. 13 (2022) 918.
[16] H. Lu, et al., 3D Printing and processing of miniaturized transducers with near-pristine piezoelectric ceramics for localized cavitation, Nat. Commun. 14 (2023) 2418.
[17] G.I. Peterson, et al., Production of materials with spatially-controlled cross-link density via vat photopolymerization, ACS Appl. Mater. Interfaces 8 (2016) 29037–29043.
[18] L. Yue, et al., Single-vat single-cure grayscale digital light processing 3D printing of materials with large property difference and high stretchability, Nat. Commun. 14 (2023) 1251.
[19] X. Kuang, et al., Grayscale digital light processing 3D printing for highly functionally graded materials, Sci. Adv. 5 (2019) eaav5790.
[20] M. Zhang, et al., Voxel Design of Grayscale DLP 3D-Printed Soft Robots, Adv. Sci. (2024) 2309932.
[21] L. Yue, et al., Cold-programmed shape-morphing structures based on grayscale digital light processing 4D printing, Nat. Commun. 14 (2023) 5519.
[22] M.M. Emami, M. Jamshidian, D. Rosen, Multiphysics modeling and experiments of grayscale photopolymerization with application to microlens fabrication, J. Manuf. Sci. Eng. 143 (2021) 091005.
[23] M.M. Emami, D.W. Rosen, Modeling of light field effect in deep vat polymerization for grayscale lithography application, Addit. Manuf. 36 (2020) 101595.
[24] E. Guven, Y. Karpat, M. Cakmakci, Improving the dimensional accuracy of micro parts 3D printed with projection-based continuous vat photopolymerization using a model-based grayscale optimization method, Addit. Manuf. 57 (2022) 102954.
[25] S.M. Montgomery, F. Demoly, K. Zhou, H.J. Qi, Pixel-Level Grayscale Manipulation to Improve Accuracy in Digital Light Processing 3D Printing, Adv. Funct. Mater. 33 (2023) 2213252.
[26] S.M. Montgomery, C.M. Hamel, J. Skovran, H.J. Qi, A reaction–diffusion model for grayscale digital light processing 3D printing, Extrem. Mech. Lett. 53 (2022) 101714.
[27] S.M. Montgomery, et al., Locally patterned anisotropy using grayscale vat photopolymerization, Addit. Manuf. 73 (2023) 103687.
[28] C. Zhou, H. Xu, Y. Chen, Spatiotemporal Projection-Based Additive Manufacturing: A Data-Driven Image Planning Method for Subpixel Shifting in a Split Second, Adv. Intell. Syst. 3 (2021) 2100079.
[29] T.J. Kolibaba, et al., Results of an interlaboratory study on the working curve in vat photopolymerization, Addit. Manuf. 84 (2024) 104082.

[30] J.H. Lee, R.K. Prud'homme, I.A. Aksay, Cure depth in photopolymerization: Experiments and theory, 3536-354, J. Mater. Res. 16 (2001), 3536-354.
[31] Y. Rudenko, A. Lozovaya, L. Asanova, N. Fedyakova, P. Chapala, Light intensity influence on critical energy and penetration depth for vat photopolymerization technology, Prog. Addit. Manuf. 9 (2024) 553–561.
[32] K. Billerbeck, C. Hägele, J. Träger, Relation of the working curve and exposure intensity in VPP 3D-printing, Prog. Addit. Manuf. 9 (2024) 1015–1023.
[33] A. Vitale, M.G. Hennessy, O.K. Matar, J. o T. Cabral, Interfacial profile and propagation of frontal photopolymerization waves, Macromolecules 48 (2015) 198–205.
[34] J. Wu, et al., Reversible shape change structures by grayscale pattern 4D printing, Multifunct. Mater. 1 (2018) 015002.
[35] K.L. Sly, T.T. Nguyen, J.C. Conboy, Lens-less surface second harmonic imaging, Opt. Express 20 (2012) 21953–21967.
[36] H. Hingorani, Y.-F. Zhang, B. Zhang, A. Serjouei, Q. Ge, Modified commercial UV curable elastomers for passive 4D printing, Int. J. Smart Nano Mater. 10 (2019) 225–236.
[37] H. Gong, B.P. Bickham, A.T. Woolley, G.P. Nordin, Custom 3D printer and resin for 18 μm× 20 μm microfluidic flow channels, Lab a Chip 17 (2017) 2899–2909.
[38] Y. Shan, A. Krishnakumar, Z. Qin, H. Mao, Reducing lateral stair-stepping defects in liquid crystal display-based vat photopolymerization by defocusing the image pattern, Addit. Manuf. 52 (2022) 102653.
[39] J. Wu, et al., Evolution of material properties during free radical photopolymerization, J. Mech. Phys. Solids 112 (2018) 25–49.
[40] J. Bonada, A. Muguruza, X. Fernández-Francos, X. Ramis, Optimisation procedure for additive manufacturing processes based on mask image projection to improve Z accuracy and resolution, J. Manuf. Process. 31 (2018) 689–702.